Multiyear Arctic Sea Ice Classification Using QuikSCAT

Aaron M. Swan and David G. Long, *Fellow, IEEE*

***Abstract*—Long-term trends in Arctic sea ice are of particular interest in studies of global temperature, climate change, and industrial application. This paper analyzes intra-annual and interannual trends in Ku-band backscatter over first-year (FY) and multiyear (MY) sea ice to develop a new sea-ice-type classification method. Histograms of backscatter are derived from high-resolution backscatter images created using the scatterometer image reconstruction (SIR) algorithm applied to measurements obtained by the SeaWinds instrument aboard QuikSCAT. The backscatter of FY and MY sea ice are clearly identifiable and are observed to vary seasonally. Using an average of the annual backscatter trends obtained from QuikSCAT, a classification of MY ice is obtained, which uses a time-dependent threshold value. Validation of the classification method is done using regional ice charts from the Canadian Ice Service. Differences in ice classification are found to be less than 6% for the winters of 2006–2007 and 2007–2008, and the end of 2008. Anomalies in the distribution of sea ice backscatter from year to year suggest a reduction in MY ice cover between 2003 and 2009 and an approximately equivalent increase in FY ice cover.**

***Index Terms*—Ice classification, microwave remote sensing, QuikSCAT, sea ice.**

I. Introduction

THE HIGH albedo and insulating properties of sea ice make it climatically influential [1]. Changes in the Arctic ice cover influence shipping navigation routes, unique ecosystems above and below the ice, and the exploration of untapped gas and oil reserves [2]. The coverage of perennial or multiyear (MY) ice is of particular interest due to its greater thickness and higher albedo over seasonal or first-year (FY) ice [3]. It poses both more stability to the ice cover and more danger to sea vessels than FY ice [4].

In order to characterize changes in sea ice, a wide variety of tools are commonly used. These include observations from ships, buoys, aircraft, and satellites. Satellite-borne microwave sensors have been used in various studies to estimate sea ice concentration and extent [1], [5]–[9] as well as to classify sea ice as FY or MY [10]–[12].

Manuscript received April 29, 2011; revised November 3, 2011; accepted January 8, 2012. Date of publication February 7, 2012; date of current version August 22, 2012.

A. M. Swan is with ImSAR, Springville, UT 84663 USA (e-mail: aaronmswan@gmail.com).

D. G. Long is with the Department of Electrical and Computer Engineering, Brigham Young University, Provo, UT 84602 USA (e-mail: long@ee.byu.edu).

Color versions of one or more of the figures in this paper are available online at http://ieeexplore.ieee.org.

Digital Object Identifier 10.1109/TGRS.2012.2184123

Sea ice is, in general, very dynamic both intra-annually and interannually. In 2010, Arctic *sea ice extent*, which includes sea ice concentrations above 15%, fluctuated between 15.25 and 4.6 million km^2 [13]. Kwok *et al.* [14] report findings of interannual MY sea ice loss through a study of ice thickness. In their study, a five-year period from 2003 to 2008 was investigated during which ice draft profiles were obtained from a submarine cruise and moorings in the Chukchi and Beaufort seas. Additional estimations of the ice draft were made using a laser altimeter aboard ICESat to retrieve elevation data over the Arctic Ocean. The study concluded that, in the 4 years following 2005, there was a net loss in MY sea ice volume of 6300 km^3, which corresponds to a 42% decrease.

In terms of ice classification, microwave backscatter has been found to produce more temporally stable results than microwave brightness temperature [10]. In another study by Kwok [12], FY ice and MY ice are classified using a fixed threshold on Ku-band backscatter obtained from the SeaWinds instrument aboard QuikSCAT. The threshold is determined to be optimal by visual inspection with collocated high-resolution RADARSAT imagery. In a separate study by Nghiem *et al.* [15], Arctic sea ice is classified as seasonal, perennial, and mixed ice also using SeaWinds measurements. Although the published literature on their method is sparse, it is clear that the classifications are based on statistical analysis, noting that seasonal ice and perennial ice have distinct backscatter signatures. Their results were validated using observations from an icebreaker in the Barents Sea during October and November of 2001.

In this paper, we develop a seasonally varying threshold to discriminate between FY and MY ice during the winter. Similar to [12], backscatter measurements from the SeaWinds instrument aboard QuikSCAT are used to classify Arctic sea ice as FY or MY ice. The classification is derived from observed trends in SeaWinds measurements over a period of seven years. These trends provide insight into the backscatter signatures of aging sea ice. The resulting classification indicates that the coverage of MY ice has reduced from year to year relative to FY ice between 2003 and 2009, as was previously reported in [14].

The rest of this paper is organized as follows. Section II provides background on the active and passive microwave data used to study the trends of FY and MY ice, where microwave data extend over a common time period from 2003 to 2009. Passive microwave data are used to isolate regions of high ice concentrations in Section III. These regions are further analyzed in Section IV, where trends in FY and MY ice are discussed. These trends lead to a method of classification presented in Section V. Classification results are validated against Canadian

Ice Service (CIS) charts in Section VI. Typical classification results and a discussion of MY ice loss are presented in Section VII.

II. Data Sources

The National Aeronautics and Space Administration (NASA) launched the SeaWinds instrument aboard QuikSCAT in 1999 [16] as a quick replacement for the NASA Scatterometer, which failed in 1997. SeaWinds (hereafter referred to as QuikSCAT by convention) employs a rotating pencil beam antenna which transmits and receives at 13.4 GHz. Measurements of the normalized backscatter cross section (σ^0) are collected in horizontal (HH) and vertical (VV) polarizations at incidence angles of 46° and 54.1°, respectively. QuikSCAT achieved global daily coverage for ten years, producing a consistent and nearly uninterrupted data set over its period of operation. In 2009, its rotating antenna stalled, limiting further observations. Although QuikSCAT was designed to measure wind speed and direction over the ocean, the radar backscatter measurements collected are sensitive to land, snow, water saturation, and various types of ice.

The QuikSCAT data used in this paper have been processed using the scatterometer image reconstruction (SIR) algorithm [17], [18]. QuikSCAT SIR images are provided in log scale at two resolutions referred to as "egg" and "slice," where egg and slice are references to the antenna footprint. Egg-based SIR images have a nominal pixel resolution of 4.45 km with an estimated effective resolution of ∼8–10 km. Slice-based SIR images have a nominal pixel resolution of 2.225 km with an estimated effective resolution of ∼5 km. The QuikSCAT egg images used in this paper are of lower resolution than slices but are less noisy. These daily polar SIR images are produced in a polar stereographic map projection.

To derive the ice classification algorithm for QuikSCAT data, a mask is applied to remove measurements over ocean and low concentrations of sea ice. The Advanced Microwave Scanning Radiometer of NASA's Earth Observing System (AMSR-E) is selected for this purpose and additionally provides a passive complement to QuikSCAT data. AMSR-E was developed by the National Space Development Agency of Japan and launched in 2002. The hardware improvements over existing spaceborne radiometers include the largest main reflector of its kind and the addition of 6.9-GHz channels. AMSR-E is currently operational and provides measurements over 6 frequencies ranging from 6.9 to 89.0 GHz. Measurements are taken at vertical and horizontal polarizations at each frequency for a total of 12 channels [19]. As with QuikSCAT, AMSR-E is in a sun-synchronous orbit and provides consistent daily coverage of the poles. The brightness temperatures obtained are sensitive to land, snow, ice, and water. AMSR-E is also available in a SIR image format using a variation of the SIR algorithm [17], [20].

III. Filtering Low-Sea-Ice-Concentration Pixels in QuikSCAT Data

For the purposes of developing a model, we exclude backscatter measurements over open water and low sea ice concentrations. This initial step effectively excludes the marginal ice zone (MIZ) where open ocean processes (particularly waves) significantly influence the backscatter in this zone. Although QuikSCAT measurements are sensitive to the ocean–ice interface, high winds often cause measurements over the ocean to appear like ice. High winds can make it difficult to isolate high ice concentrations using QuikSCAT. However, brightness temperatures obtained from the 6-GHz V (or H) channel of AMSR-E $(A_{6,V})$ show a high contrast between ocean and ice. AMSR-E SIR images have high resolution (nominally 8.9 km/pixel for the 6-GHz channel) and span largely the same time frame as QuikSCAT. They are also readily available and are collocated with QuikSCAT SIR images. The contrast between open water and FY ice, with respect to emissivity (and brightness temperature), increases as frequency decreases [21]. Applying a fixed threshold to $A_{6,V}$ is a simple and adequate method to remove measurements over the ocean and the MIZ. Using one of the previously mentioned sea ice concentration algorithms may also be appropriate for this purpose.

To illustrate the sensitivity of $A_{6,V}$ to sea ice concentration, a comparison is made with ice concentration maps produced by the NASA Team (NT) sea ice algorithm [22], [23]. The NT ice concentrations (which are provided in polar stereographic projection) were resampled using bilinear interpolation for comparison. Fig. 1 shows the typical joint histograms of NT ice concentrations and $A_{6,V}$ measurements from 2004. In each case, a high correlation between $A_{6,V}$ and the NT ice concentration is evident. Areas with $A_{6,V}$ brightness temperatures above 220 K correspond to winter sea ice concentrations of 40% or more. For illustration, the 220 K threshold is shown in Fig. 1 (and later in Fig. 3). We note here that the observed distributions of QuikSCAT measurements corresponding to pixels above the threshold are not sensitive to the exact threshold on $A_{6,V}$.

An advantage of using only $A_{6,V}$ is its lack of sensitivity to ice type, which prevents a bias toward the selection of FY or MY ice. A typical SIR image of $A_{6,V}$ is shown in Fig. 2, where ocean and ice measure approximately 160 K and 250 K, respectively. There is no clear distinction between FY and MY ice at this frequency. For reference, MY ice is typically located north of Greenland's coast and in the vicinity of the north pole. Fig. 3 shows a time series of histograms during 2004 of $A_{6,V}$. By visual comparison with $A_{6,V}$ SIR images (Fig. 2 for example), the mode on the left of the figure represents ocean, while the varying mode on the right represents ice. Except during the summer (days 150 to 250), measurements over FY and MY ice are indistinguishable in $A_{6,V}$.

A typical derived sea ice mask created using this threshold approach is shown applied to a QuikSCAT SIR image in Fig. 4 for day of year (DOY) 20, 2004. Ocean has been removed by the mask. Land has been removed using a standard Arctic land mask.

IV. Temporal Trends Observed in QuikSCAT Measurements

During the winter, active microwave measurements from QuikSCAT are characteristically brighter over MY ice while lower returns are seen over FY ice. Some of the distinction between ice types is due to differences in ice salinity, porosity,

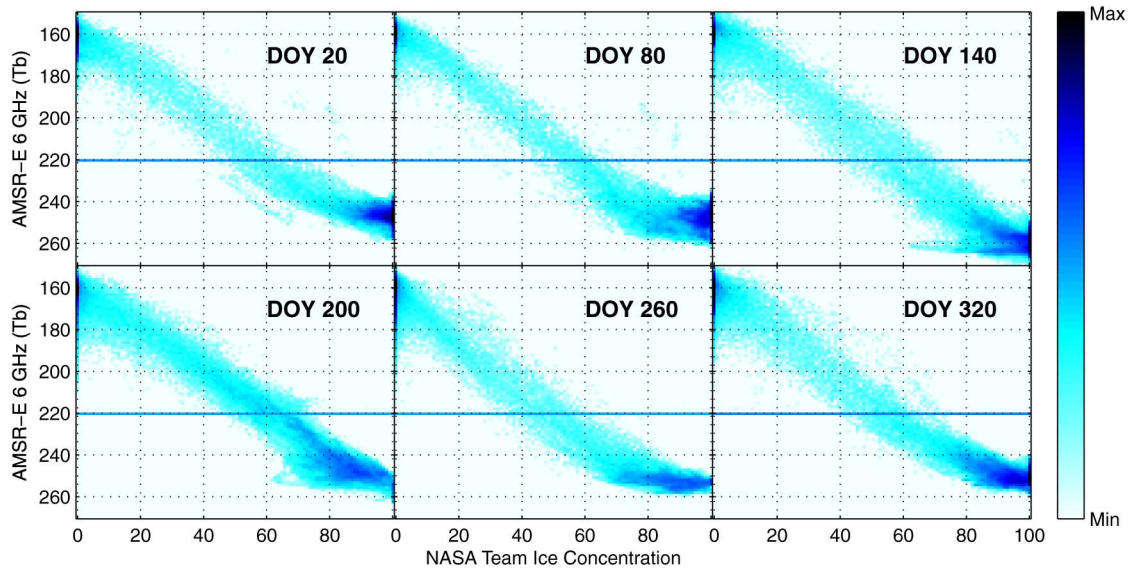

Fig. 1. Typical joint histograms of AMSR-E 6-GHz V brightness temperatures and ice concentrations from the NT algorithm for selected DOYs in 2004. Histogram bins have been log height scaled. The horizontal line represents a threshold at 220 K.

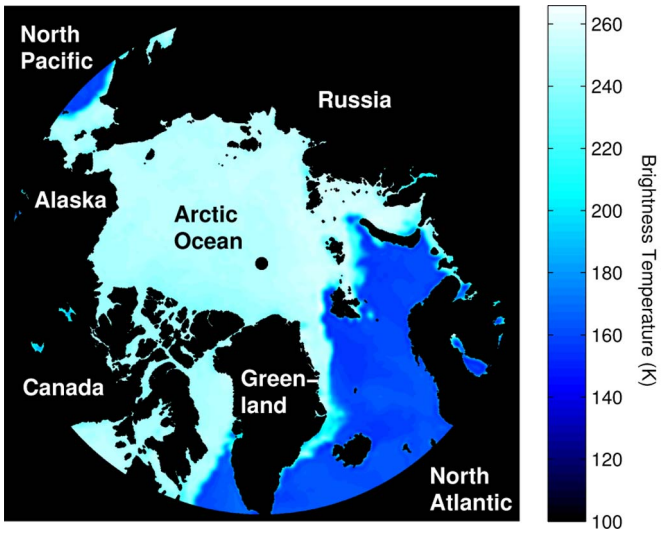

Fig. 2. AMSR-E 6-GHz V brightness temperatures (in kelvins) over the Arctic on DOY 32, 2005 (land has been excluded). The ocean and ice measure approximately 160 K and 250 K, respectively.

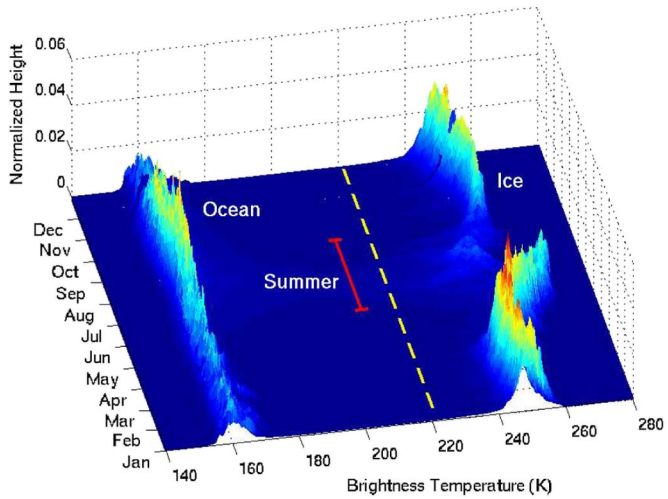

Fig. 3. Daily time series of histograms of AMSR-E 6-GHz V brightness temperatures over the Arctic during 2004. Histograms are normalized and exclude measurements over land. The dashed line represents a threshold separating modes representative of ocean and ice. The summer melt period is indicated by the solid line.

surface roughness, ridges on the order of meters to kilometers in length, and the properties of snow cover. Analyses of satellite scatterometer data show a large dynamic range of Ku-band backscatter, which has a strong sensitivity to FY and MY ice [15].

Understanding the temporal nature of sea ice backscatter allows and/or improves the classification of ice as FY or MY. To visualize temporal sea ice characteristics, we use a time series of histograms of QuikSCAT measurements. Fig. 5 shows a series of histograms for the winter of 2006–2007, where sea ice has been selected using the method described in Section III and the histograms have been normalized. The distribution from each day during the winter has approximately one large mode around -20 dB representing FY ice and one large mode around -10 dB with some smaller modes above -10 dB representing MY ice. Approximate classification of the modes is obtained by observing regions of ice which have survived the summer melt (MY ice), as well as regions of FY ice formed during the winter. Also, at Ku-band, σ^0 for FY ice is approximately -25 to -18 dB, and MY ice is approximately -10 to -12 dB [24].

A. Trends in FY Ice

Similar to Fig. 5, the winter of 2004–2005 is shown in Fig. 6(a), where the perspective is now rotated and viewed from top down. Fig. 6(a) shows evidence that the microwave signature of FY ice in combination with its snow cover is seasonally dependent. The pattern shown in Fig. 6(b) approximately describes the behavior of FY ice backscatter for every year between 2003 and 2009. The pattern is based on visual observations of the temporal progression of the distribution of backscatter each year. A statistical result could not be obtained

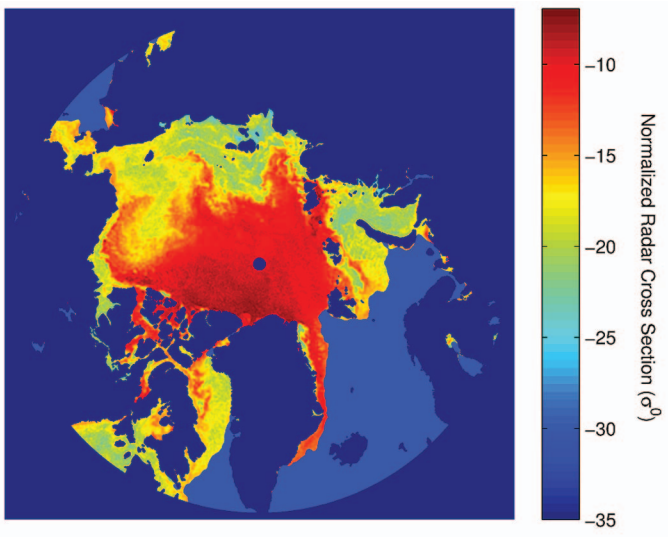

Fig. 4. Typical egg SIR image of QuikSCAT VV (σ^0 in decibels). The ocean has been masked by applying a threshold to collocated AMSR-E brightness temperatures (DOY 20, 2004).

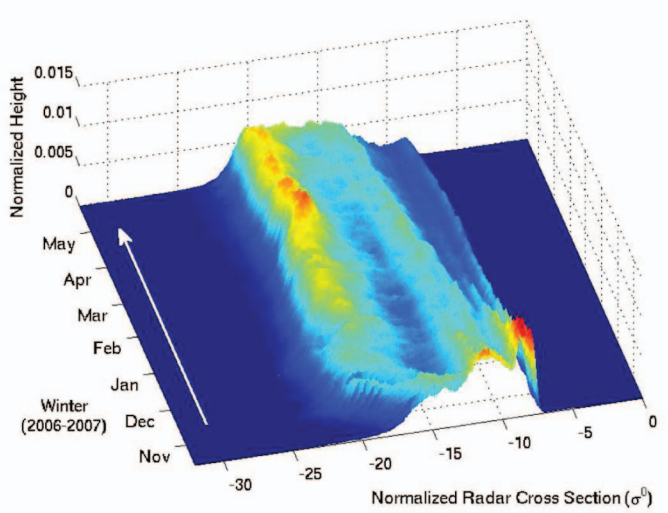

Fig. 5. Temporal series of histograms of QuikSCAT VV backscatter over sea ice during the 2006–2007 winter. The white arrow indicates temporal progression. Color indicates normalized height.

due to the limited availability of other MY ice classifications. Observations suggest that FY ice backscatter quickly moves to lower values between September and mid-November. It decreases slightly (sometimes, remaining constant) during December and January and then gradually moves to higher values until mid-March. After March, the backscatter moves to lower values until June. Then, it becomes difficult to distinguish the ice type by backscatter until late September due to melting. After September, new ice forms. The variability of the FY ice trend is influenced by several factors. Some of these include new ice formation, brine drainage, ridging and rafting of ice sheets, snow metamorphism under different meteorological conditions, ice growth rate (which affects ice salinity), and atmospheric and ocean temperature fluctuations (which affect ice growth).

The backscatter signature of FY ice, in Fig. 6(a), seems to stabilize by mid-November. The high backscatter of FY ice

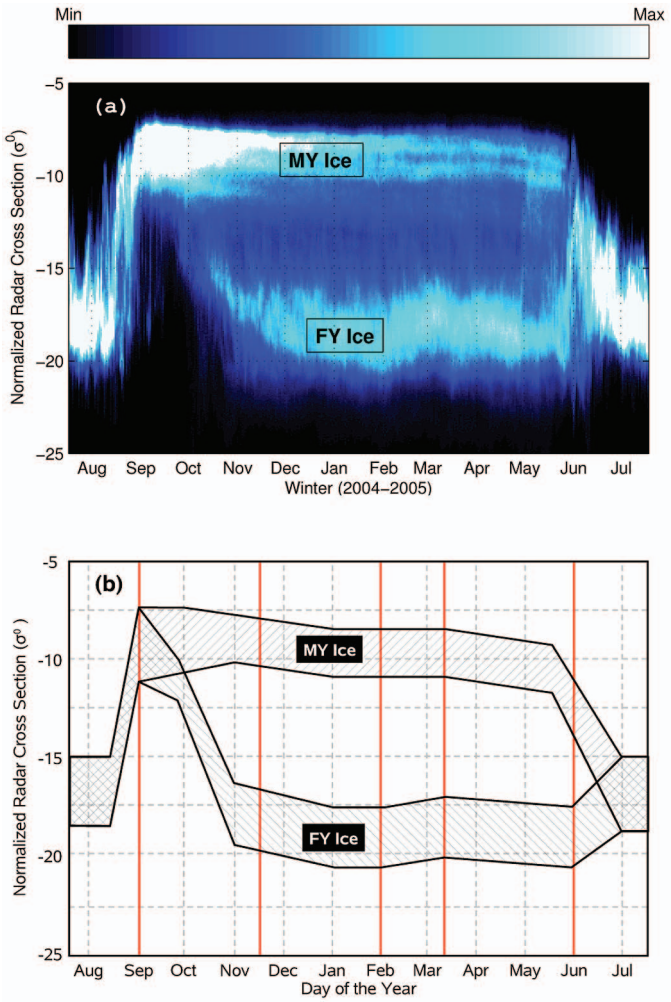

Fig. 6. Seasonal trends in backscatter over FY and MY ice. (a) Time series of histograms of backscatter over Arctic sea ice for the winter of 2004–2005. (b) Cartoon showing approximate (nonstatistical) ranges of backscatter for FY and MY ice for each year between 2003 and 2009. The range of backscatter for each ice type appears to be seasonally dependent.

observed prior to mid-November may be partially explained by frost flowers, which are formed by the deposition of ice directly from the vapor phase. Frost flowers have been seen in connection with a sharp increase in backscatter for ice that is 10 to 30 cm thick. The backscatter of this FY ice may be as high as that typically seen for MY ice. As the ice thickens, the backscatter decreases by roughly 5 to 7 dB and stabilizes to commonly observed values for FY ice [25], [26]. The gradual backscatter increases observed from February to mid-March may be accounted for by brine drainage and roughening of the surface over time. Brine drainage, which begins immediately after ice forms, leads to lower brine volume and consequently lower electromagnetic absorption. The effects of drainage, in combination with increased roughness and snowfall over time, tend to increase scattering [26]. Factors in the subsequent decrease in backscatter may be related to an increase in snow density, as discussed later.

B. Trends in MY Ice

Referring to Fig. 6(a), the backscatter signature of MY ice during the 2004–2005 winter is seasonally dependent. Over

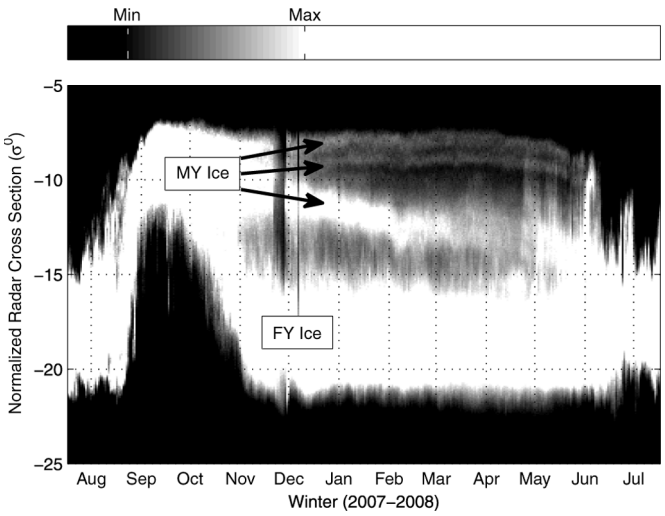

Fig. 7. Time series of histograms of QuikSCAT VV measurements over sea ice during the 2007–2008 winter. The gray scale emphasizes that multiple modes are present in the typical range for MY ice.

the winter, it moves to lower backscatter values with the exception of a pause during January and February. Reduction in MY backscatter might be due, in part, to snow accumulation and/or increasing snow density. Arctic snow accumulation is the greatest in the fall, with little accumulation in December and January and then gradually increasing accumulation in spring until May [27].

The pattern of snowfall seems to mimic the pattern of decreasing backscatter, suggesting a possible connection. The average snow density in the Arctic has been observed to gradually increase during the winter over MY ice [27]. Under dry snow conditions, snow density, grain size, and stratification are the dominant factors in determining the backscatter coefficient, which is inversely correlated with snow density [28]. In distinguishing ice type by backscatter, there is an implied assumption that backscatter increases as ice ages. In 2004 and later, the mode representing MY ice splits into as many as three or more distinguishable modes. An example of these modes is shown in Fig. 7 for the 2007–2008 winter. In the following, we show that σ^0 generally increases (to an upper limit) for MY ice after each summer melt.

To study this increase, σ^0 measurements are collocated with the position of buoys deployed in MY ice by the Cold Regions Research and Engineering Laboratory (CRREL). The buoys allow a parcel of ice to be tracked over time. The implicit assumptions are that buoys are fixed relative to a surrounding parcel of ice, that similar ice characteristics exist within a 5-km radius (QuikSCAT egg resolution), and that temporal disparities of less than one day are acceptable. Tracking the backscatter over an ice parcel provides significant information about the time-varying characteristics of the ice. Of the more than 40 buoys deployed in the Arctic between 2003 and 2009, at least 10 remained active long enough to provide MY comparisons.

Typical plots for collocated σ^0 VV measurements for various time periods are shown in Fig. 8, where corresponding buoy tracks are shown below each plot. Very similar results were obtained using σ^0 HH. CRREL buoy 2005E, which is shown in Fig. 8(a), was deployed on MY ice at 83 N, 174 W as part of the Healy–Oden Trans-Arctic Expedition (HOTRAX). It traveled toward the north coast of Greenland for two years. Collocated σ^0 VV measurements show an increase of about 2 dB between the winters of 2005–2006 and 2006–2007. Buoy 2006C in Fig. 8(b) was deployed in the Beaufort Sea by the Woods Hole Oceanographic Institution. It initially shows a decrease in σ^0 during 2007. However, after the buoy heads out of the Beaufort Gyre, σ^0 increases by about 4 dB between the winters of 2007–2008 and 2008–2009. Although very few data are available for the winter of 2009–2010, there is some indication of an additional increase of about 2 dB. Buoy 2006F, which was deployed in the Laptev Sea, is shown in Fig. 8(c). Collocated measurements show an increase of about 4 dB between the end of 2006 and the end of 2007. The trailing-off backscatter value at the end of 2007 may be a result of mixed FY and MY ice as the buoy heads out of the Fram Strait. Another possibility may be heavy snowfall, causing the ice floe to be flooded with seawater. This flooding has been previously noted to occur in the Fram Strait [25].

The only case studies of collocated σ^0 and buoy positions not exhibiting an increase in σ^0 are found in the Beaufort Sea. Buoy 2007J, shown in Fig. 8(d), shows steady σ^0 values for the winter of 2007–2008, but then decreasing values for the remaining life of the buoy. The observed decrease might be attributed to mixing of FY and MY ice in the Beaufort Gyre, with the possible melting of the ice parcel during the last year of buoy activity. Collocated measurements over three additional buoys (2005B, 2007E, and 2007F) also show decreasing backscatter as each buoy track heads into the Beaufort Gyre. Buoy 2005B survives long enough to exit the gyre and show a postsummer increase in 2007 backscatter in comparison to 2006 backscatter. Collocated measurements over six additional buoys show postsummer increases in backscatter over the previous year.

While it is difficult to determine the cause of increased backscatter of MY ice in all cases, a possible explanation follows. Microwave scattering results from a combination of surface and volume scatterers. Volume scattering from MY ice is largely a result of air pockets and channels within the ice. During the formation of MY ice in the summer, temperature increases in the upper layers of the ice cause brine pockets to enlarge. The enlarged pockets then tend to coalesce and form a vertical network of channels in the ice. When freshwater melt forms on the surface of the ice, it contributes to this network of channels as it percolates through the ice sheet. This process reduces the salinity of the upper 50 to 100 cm of ice to less than 1‰. These changes are a major contributing factor to the large backscatter increase of MY ice over FY ice [25]. Percolation of freshwater melt occurs each year, which may cause widening of—or additions to—the vertical network of channels within the ice sheet. Increased porosity of the ice could account for increased volume scattering.

C. Interannual Trends in Sea Ice Coverage

Interannual trends in sea ice may be observed by analyzing the distribution of σ^0 over a period of several years. Fig. 9(a) shows a plot of daily histograms of normalized backscatter from 2003 to 2009. Fig. 9(b) shows the total area of ice isolated for

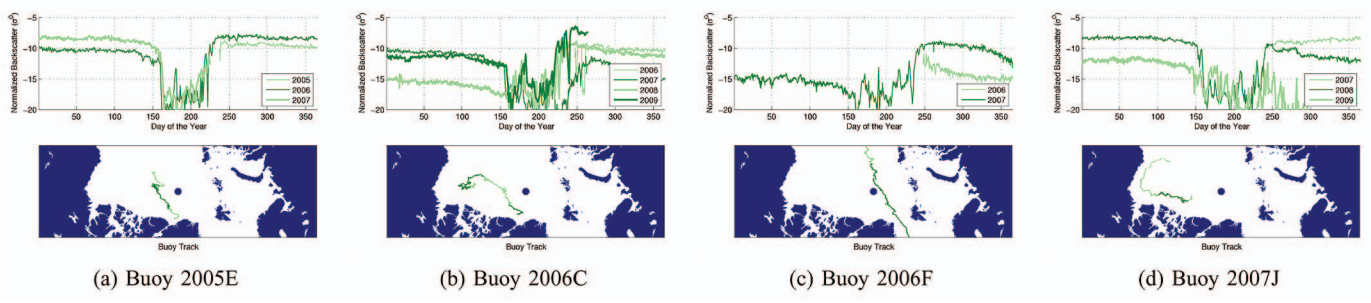

Fig. 8. (Above) Typical results for collocated σ^0 VV measurements and CRREL buoys, and (below) buoy positions. (a) Buoy 2005E. (b) Buoy 2006C. (c) Buoy 2006F. (d) Buoy 2007J.

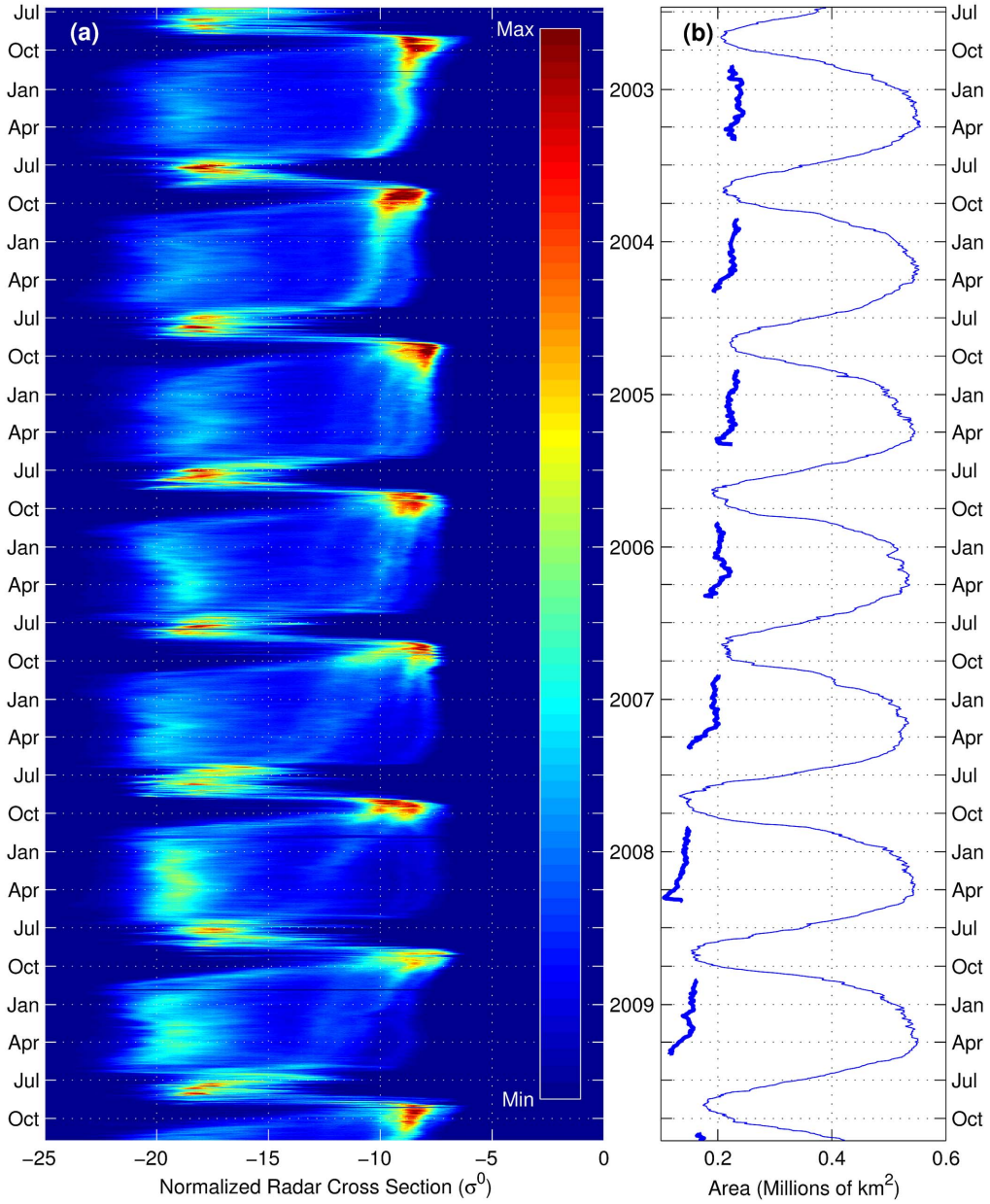

Fig. 9. (a) Temporal series of histograms of QuikSCAT VV measurements over sea ice and (b) (thin line) the total area of ice above the $A_{6,V}$ 220 K threshold for each day as well as (thick line) the total area of MY ice during the winter using the classification method described later in this paper.

each day. It shows that the total area of ice under consideration is seasonally consistent. These histograms suggest a gradual shift in the ice cover from MY to FY ice. The MY ice mode (right) becomes progressively weaker and dispersed during this period, while the FY ice mode (left) becomes progressively stronger. Since Fig. 9(a) shows that the area of sea ice under

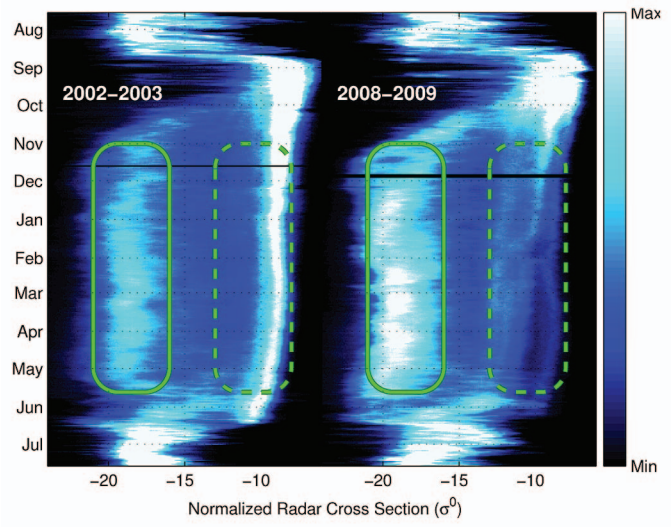

Fig. 10. Plot of backscatter versus time for two different winters. The winter of 2002–2003 is shown on the left, and that of 2008–2009 is shown on the right. The FY ice mode is marked by the solid line, and the MY ice mode by the dashed line for each winter. Note that MY ice distributions are brighter during the winter of 2002–2003 and FY ice distributions are brighter during the winter of 2008–2009.

consideration does not change significantly from winter to winter, we conclude that MY ice has gradually been replaced by FY ice over this period. We note that there is some indication of a possible rebound of this trend in 2009. In addition, it should be noted that the minimum ice areas given in Fig. 9(b) may be inaccurate due to summer melt conditions.

To illustrate the shift in sea ice cover from MY to FY ice, Fig. 10 shows the daily histograms of backscatter during the winters of 2002–2003 and 2008–2009. There is a clear increase in FY ice, highlighted by the solid line, as well as a clear decrease in MY ice, highlighted by the dashed line. Selected SIR images from QuikSCAT VV are shown in Fig. 11 to provide a spatial confirmation of this pattern.

V. MY Ice Classification

The trends observed in sea ice backscatter for FY and MY ice appear to be interannually consistent. Each year, there is a clear separation of FY ice and MY ice. FY ice has some variations that may be due to snowfall or other weather events, but the variations are reasonably small with respect to the larger trends in ice type. For MY ice, the number of observed trends in backscatter depends on the year. The appearance of different signatures from year to year may be explained by the varying spatial coverage of MY ice of different ages. CRREL Buoy 2006F [Fig. 8(c)], which was deployed in MY ice, gives evidence that MY ice may return backscatter signatures as low as -15 dB.

These observations give rise to a method for FY/MY ice classification using an average of the yearly distributions. Fig. 12(a) shows the histograms of σ^0 VV for an annual period averaged over 7 years (2003–2009). The scales of the image are adjusted to show a minimum bin count that exists over most of the winter, which separates distributions associated with FY and MY ice. A threshold model, which is dependent on the DOY, is selected by fitting a curve to the minimum of each histogram during the winter. Artificial bounds, which are shown in 12(b), are used to approximately isolate the daily minimum. The minimum found between these bounds and the fitted curve are also shown in Fig. 12(b). A fifth-degree polynomial is fitted using a least squares method. Although seasonal changes in the data are naturally periodic, a polynomial fit locally approximates periodic data and can be fitted to seasonal changes. Backscatter values below this threshold are classified as FY ice, and those above this threshold are classified as MY ice.

A limitation of this classification method is that MY ice can sometimes look like FY ice. Comiso suggests that ice floes near the MIZ that survive the summer melt often have passive microwave signatures similar to FY or intermediate ice later in the winter. He suggests that this is due to the intrusion of seawater into the snow–ice interface during the summer [29]. This intrusion affects active microwave signatures due to the salty ocean water entering the porous upper layers of the ice. It has been observed that microwave signatures of flooded MY ice can easily be confused with FY ice. In the Fram Strait, Tucker *et al.* found that surface flooding was observed on about 30% of sampled ice floes [25]. In some instances, FY ice looks like MY ice if it has undergone significant rafting and ridging and/or brine exclusion. While we have excluded the MIZ for the purpose of deriving our sea ice classification, we mention this limitation for completeness.

VI. Validation

Ice charts from the CIS [30] are used to validate the classification of FY and MY ice. These charts are based on an analysis and an integration of several data sources, including weather and oceanographic information; *in situ* observations from land, ship, and aircraft; airborne radar; and satellite imagery. We note that validation using these charts may not be completely independent due to the use of satellite data. In addition, we note the availability of similar charts produced by the National Ice Center. Regional ice charts provide an analysis of ice conditions for a given region and date, where data up to three days prior are used to determine ice concentration, stage of development, and ice form, following World Meteorological Organization terminology. Ice charts have been available on a weekly (sometimes biweekly) basis since 2006. For validation, the most useful regions are the Western Arctic and Eastern Arctic. These regions are commonly covered by FY and MY ice. The regions themselves are divided into approximately homogeneous subregions and assigned a total ice concentration. The three most prominent ice types within the subregion are recorded with their partial concentration, stage of development and thickness, and form or floe size. The sum of the partial ice concentrations is always less than or equal to the total ice concentration for the subregion. The data for each subregion are contained in an oval chart typically referred to as an egg code.

In order to compare CIS ice charts with FY and MY ice classifications derived from QuikSCAT backscatter, ice chart stages surviving at least one melt season (old ice, second-year ice, and MY ice) are grouped as MY ice, and all other ice types

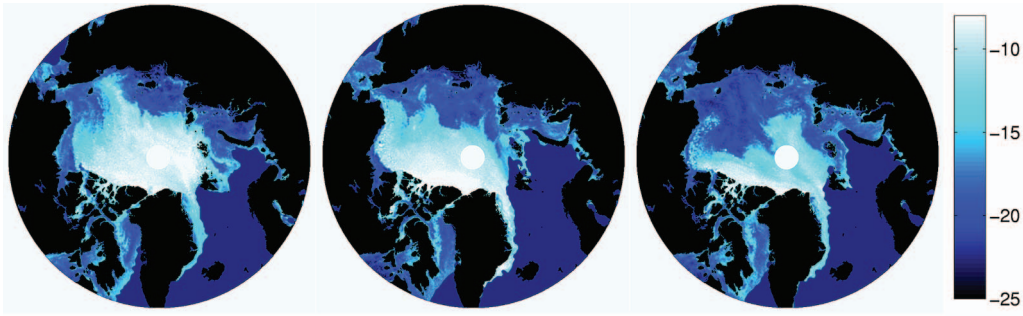

Fig. 11. Selected QuikSCAT VV (σ^0 in decibels) images showing trend in decreasing MY ice from 2003 to 2009. Images from left to right represent DOY 32, in 2003, 2006, and 2009. Land is shown as black, and ocean is dark blue. Brighter colors correspond to increased backscatter, where FY is approximately below −15 dB and MY is above.

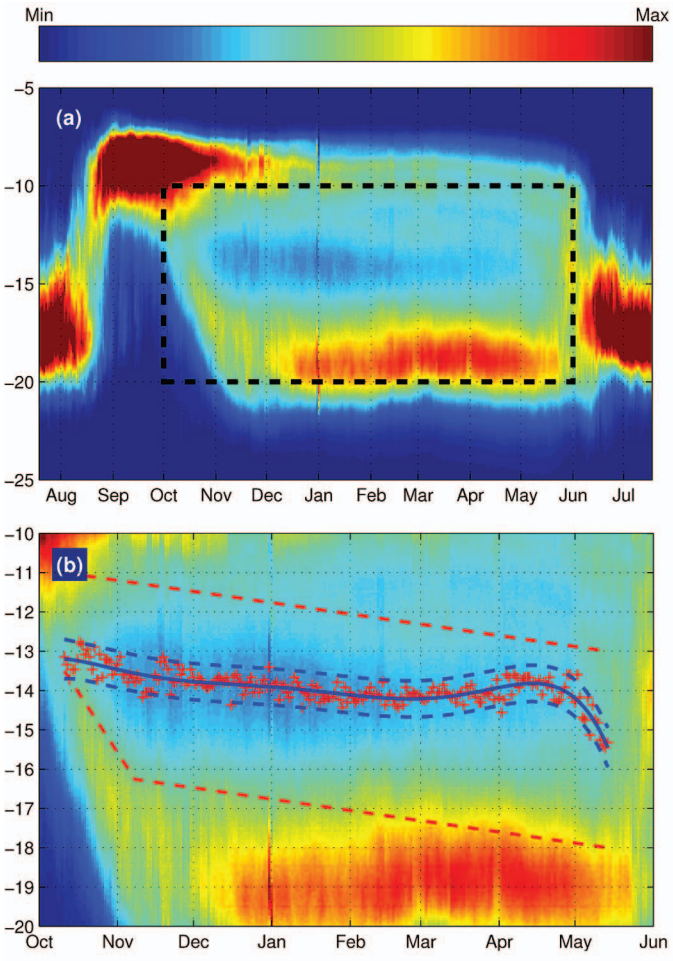

Fig. 12. (a) Annual time series of daily histograms averaged over 7 years (2003–2009). The dashed box represents a subset shown in (b). (b) Classification threshold on QuikSCAT backscatter distributions. Shown are (dashed straight lines) bounds set to the minimum, (+) the minimum found for each DOY, and (solid curve) a curve fitted to the results with (dashed curves) 95% confidence intervals.

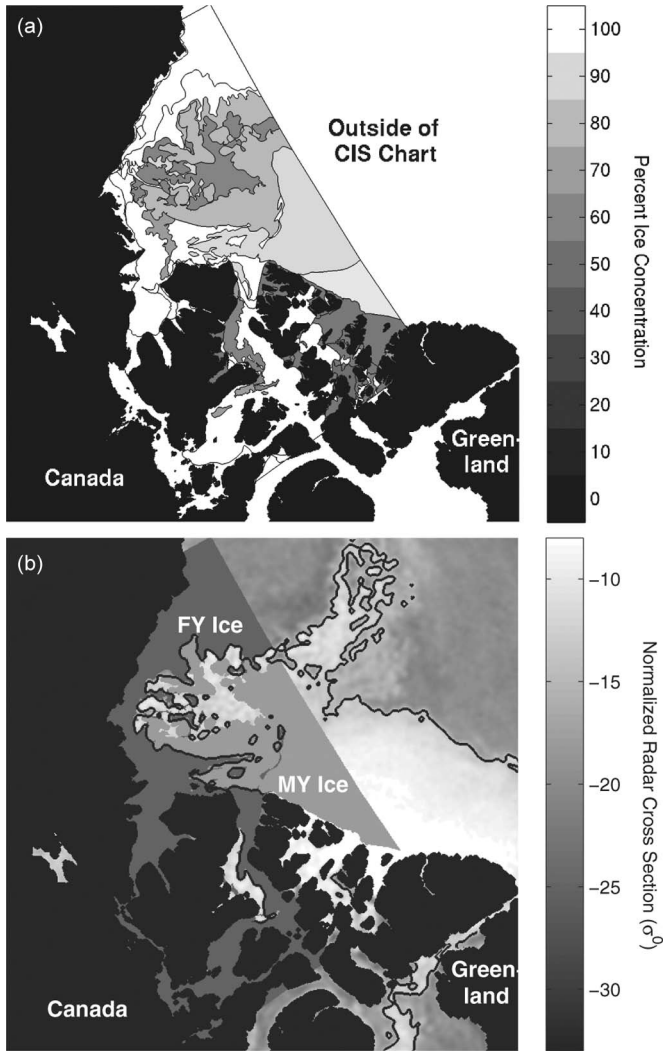

Fig. 13. Collocated CIS Western Arctic ice chart and QuikSCAT SIR image on DOY 42, 2008. The black color represents land. (a) Percent ice concentration for the highest ice stage concentrations for each ice chart subregion. (b) Ice stage concentrations above 70% grouped as FY or MY ice overlaid on a QuikSCAT SIR image (σ^0 in decibels). The black line represents the classification threshold between FY and MY ice.

are grouped as FY ice. For the purpose of comparison, the ice stage within a subregion with the highest partial ice concentration is assumed to represent the whole subregion. In order to counter the error that may be introduced by this assumption, only subregions in which the highest partial ice concentration is 70% or greater are considered. The next highest partial ice concentration for these subregions is less than 30% by definition and is assumed to make little contribution. When a range of partial ice concentrations is specified in the CIS ice charts, the average is used. For example, for the partial ice concentration of 60%–80%, a value of 70% is assumed. Each

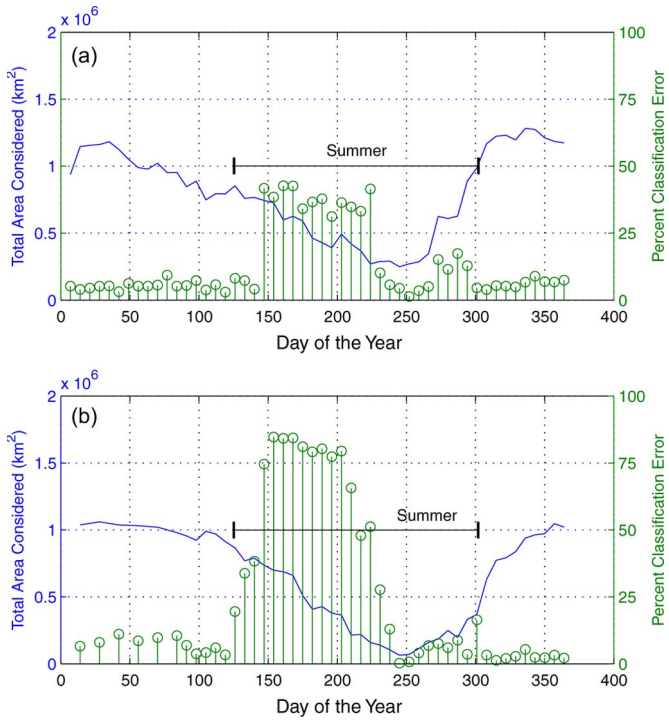

Fig. 14. Classification error using CIS ice charts. The error represents the percentage of ice cover misclassified using QuikSCAT σ^0 for the (a) Western Arctic and (b) Eastern Arctic regions. (Solid line) The total area of ice considered and (stem plot) the error for each day are shown. The summer as indicated has been excluded from average error calculations.

ice chart region is formatted as a shape file in SIGRID-3 format with the latitude and longitude specified for the vertices of each shape. Fig. 13 shows the Western Arctic CIS ice chart region collocated with QuikSCAT VV on DOY 42, 2008. In Fig. 13(a), subregions within the ice chart are colored by the percent ice concentration of the ice stage with the highest concentration. Fig. 13(b) shows ice stages grouped as FY or MY ice overlaid on a QuikSCAT SIR image. The CIS ice chart appears to be a natural extension of the QuikSCAT SIR image.

For the winters (November, DOY 308, through April, DOY 120) of 2006–2007, 2007–2008, and the end of 2008 (DOY 308 and on), the total average error for the Western Arctic and Eastern Arctic regions is $5.84\% \pm 3.52\%$ error. For illustration, the classification error for 2008 is shown in Fig. 14(a) and (b) for the Western Arctic and Eastern Arctic regions, respectively. Summer backscatter measurements are not classified due to the high variation in backscatter over melting snow and ice. We note that there is a slight performance difference with respect to the error between the Western Arctic and Eastern Arctic regions. With a fixed threshold of -14.5 dB on σ^0, as in [12], the total average error is $7.16\% \pm 3.75\%$ error. We conclude that, for the validation regions, a seasonally varying classification threshold performs better on average than using a fixed threshold. Further validation using CIS ice charts is limited by chart availability.

VII. Discussion of Results

Results from ice classification using QuikSCAT are shown in Fig. 15 for DOY 32, 2003, through 2009. These typical

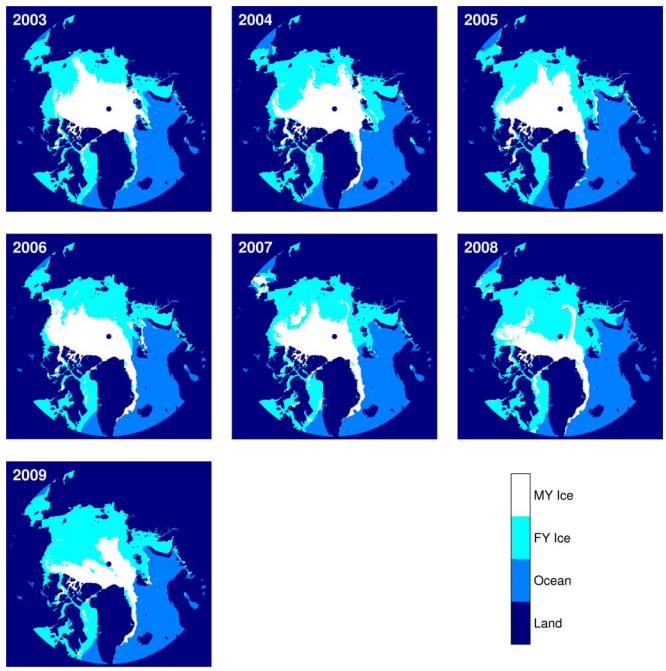

Fig. 15. Ice classification using QuikSCAT for DOY 32, 2003, through 2009. Note the trend in decreasing spatial coverage of MY sea ice.

results reveal the MY ice loss trend previously noted from the temporal trends in Fig. 9. The loss of MY ice may partially be accounted for by the advection of MY ice through the Fram Strait, as noted in multiple studies ([31] and [32] for example). The evidence presented in this paper indicates that, while the total area of highly consolidated ice has fluctuated to a small degree between 2002 and 2009, there has been a shift from MY ice to FY ice. This shift is evident using both active and passive microwave sensors. Although this trend is consistent over the selected years, it appears that, in 2009, there may be a small increase in MY ice.

VIII. Conclusion

Classifying FY and MY sea ice over the winter using a Ku-band scatterometer can be accurately accomplished using a seasonally dependent threshold to separate ice types. The results are consistent with CIS ice charts. Less than 6% average ice classification error is observed for Western and Eastern Arctic regions during the winter.

Interannual trends exist in Ku-band backscatter over FY and MY sea ice. In particular, MY ice has been observed to increase in backscatter for each melt season that it survives. The spatial coverage of MY ice is also observed to decrease significantly between 2003 and 2009. However, in 2009, there is an increase observed in the MY ice cover over the previous year.

References

[1] Q. Remund and D. Long, "Sea ice extent mapping using Ku-band scatterometer data," *J. Geophys. Res.*, vol. 104, no. C5, p. 11 515, 1999.

[2] D. Gautier, K. Bird, R. Charpentier, D. Houseknecht, T. Klett, J. Pitman, T. Moore, C. Schenk, M. Tennyson, and C. Wandrey, (2008) Circum-Arctic Resource Appraisal: Estimates of Undiscovered Oil and Gas North of the Arctic Circle. [Online]. Available: http://pubs.usgs.gov/fs/2008/3049/fs2008-3049.pdf

[3] D. Perovich, T. Grenfell, B. Light, and P. Hobbs, "Seasonal evolution of the albedo of multiyear arctic sea ice," *J. Geophys. Res.*, vol. 107, no. 8044, p. 101 029, 2002.
[4] N. Walker, K. Partington, M. Van Woert, and T. Street, "Arctic sea ice type and concentration mapping using passive and active microwave sensors," *IEEE Trans. Geosci. Remote Sens.*, vol. 44, no. 12, pp. 3574–3584, Dec. 2006.
[5] D. Cavalieri, P. Gloersen, and W. Campbell, "Determination of sea ice parameters with the Nimbus 7 SMMR," *J. Geophys. Res.*, vol. 89, no. D4, pp. 5355–5369, 1984.
[6] J. Comiso, "Characteristics of Arctic winter sea ice from satellite multispectral microwave observations," *J. Geophys. Res.*, vol. 91, no. C1, pp. 975–994, 1986.
[7] J. Comiso, "SSMI concentration using the bootstrap algorithm. NASA report 1380," *Ann. Glaciol.*, vol. 34, pp. 441–446, 1995.
[8] L. Kaleschke, G. Heygster, C. Lüpkes, A. Bochert, J. Hartmann, J. Haarpaintner, and T. Vihma, "SSM/I sea ice remote sensing for mesoscale ocean–atmosphere interaction analysis: Ice and icebergs," *Can. J. Remote Sens.*, vol. 27, no. 5, pp. 526–537, 2001.
[9] C. Swift, L. Fedor, and R. Ramseier, "An algorithm to measure sea ice concentration with microwave radiometers," *J. Geophys. Res.*, vol. 90, no. C1, pp. 1087–1099, 1985.
[10] R. Ezraty and A. Cavanié, "Intercomparison of backscatter maps over Arctic sea ice from NSCAT and the ERS scatterometer," *J. Geophys. Res.*, vol. 104, no. C5, p. 11 471, 1999.
[11] G. Belchansky and D. Douglas, "Classification methods for monitoring Arctic sea ice using OKEAN passive/active two-channel microwave data," *Remote Sens. Environ.*, vol. 73, no. 3, pp. 307–322, Sep. 2000.
[12] R. Kwok, "Annual cycles of multiyear sea ice coverage of the Arctic Ocean: 1999–2003," *J. Geophys. Res.*, vol. 109, p. C11 004, Nov. 2004.
[13] F. Fetterer, K. Knowles, W. Meier, and M. Savoie, *Sea Ice Index*. Digital Media, Boulder, CO: Nat. Snow Ice Data Center, 2009.
[14] R. Kwok, G. Cunningham, M. Wensnahan, I. Rigor, H. Zwally, and D. Yi, "Thinning and volume loss of the Arctic Ocean sea ice cover: 2003–2008," *J. Geophys. Res.*, vol. 114, no. C7, p. C07 005, Jul. 2009.
[15] S. Nghiem, Y. Chao, G. Neumann, P. Li, D. Perovich, T. Street, and P. Clemente-Colón, "Depletion of perennial sea ice in the east Arctic Ocean," *Geophys. Res. Lett.*, vol. 33, no. 17, p. L17 501, Sep. 2006.
[16] J. Huddleston and M. Spencer, "The QuikSCAT wind scatterometer mission," in *Proc. IEEE Aerosp. Conf.*, Big Sky, Montana, 2000, pp. 1–7.
[17] D. Early and D. Long, "Image reconstruction and enhanced resolution imaging from irregular samples," *IEEE Trans. Geosci. Remote Sens.*, vol. 39, no. 2, pp. 291–302, Feb. 2001.
[18] D. Long and D. Daum, "Spatial resolution enhancement of SSM/I data," *IEEE Trans. Geosci. Remote Sens.*, vol. 36, no. 2, pp. 407–417, Mar. 1998.
[19] T. Kawanishi, T. Sezai, Y. Ito, K. Imaoka, T. Takeshima, Y. Ishido, A. Shibata, M. Miura, H. Inahata, and R. Spencer, "The advanced microwave scanning radiometer for the earth observing system (AMSR-E), NASDA's contribution to the EOS for global energy and water cycle studies," *IEEE Trans. Geosci. Remote Sens.*, vol. 41, no. 2, pp. 184–194, Feb. 2003.
[20] B. Gunn, "Scatterometer image reconstruction tuning and aperture function estimation for advanced microwave scanning radiometer on the Earth observing system," M.S. thesis, Brigham Young Univ., Provo, UT, 2010.
[21] D. Eppler, L. Farmer, A. Lohanick, M. Anderson, D. Cavalieri, J. Comiso, P. Glorsen, C. Garrity, T. Grenfell, M. Hallikainen, J. Maslanik, C. Matzler, R. Melloh, I. Rubinstein, and C. Swift, "Passive Microwave Signatures of Sea Ice," in *Microwave Remote Sensing of Sea Ice*. Washington, DC: Amer. Geophys. Union, 1992.
[22] D. Cavalieri, NASA Team Sea Ice Algorithm, May 2003. [Online]. Available: http://nsidc.org/data/docs/daac/nasateam
[23] D. Cavalieri, K. St Germain, and C. Swift, "Reduction of weather effects in the calculation of sea-ice concentration with the DMSP SSM/I," *J. Glaciol.*, vol. 41, no. 139, pp. 455–464, 1995.
[24] R. G. Onstott, "SAR and Scatterometer Signatures of Sea Ice," in *Microwave Remote Sensing of Sea Ice*. Washington, DC: Amer. Geophys. Union, 1992.
[25] W. Tucker, D. Perovich, A. Gow, W. Weeks, and M. Drinkwater, "Physical Properties of Sea Ice Relevant to Remote Sensing," in *Microwave Remote Sensing of Sea Ice*. Washington, DC: Amer. Geophys. Union, 1992.
[26] M. Hallikainer and D. P. Winebrenner, "The Physical Basis for Sea Ice Remote Sensing," in *Microwave Remote Sensing of Sea Ice*. Washington, DC: Amer. Geophys. Union, 1992.
[27] S. Warren, I. Rigor, N. Untersteiner, V. Radionov, N. Bryazgin, Y. Aleksandrov, and R. Colony, "Snow depth on Arctic sea ice," *J. Clim.*, vol. 12, no. 6, pp. 1814–1829, 1999.
[28] C. Duguay and A. Pietroniro, *Remote Sensing in Northern Hydrology: Measuring Environmental Change*. Washington, DC: Amer. Geophys. Union, 2005.
[29] J. Comiso, "Arctic multiyear ice classification and summer ice cover using passive microwave satellite data," *J. Geophys. Res.*, vol. 95, no. C8, pp. 13 411–13 422, 1990.
[30] Canadian Ice Service, Canadian Ice Service Arctic Regional Sea Ice Charts in SIGRID-3 Format, Boulder, CO, USA, 2009, National Snow and Ice Data Center. Digital media.
[31] R. Kwok, G. Cunningham, and S. Pang, "Fram Strait sea ice outflow," *J. Geophys. Res.*, vol. 109, p. C09 009, Jan. 2004.
[32] I. Rigor, J. Wallace, and R. Colony, "Response of sea ice to the Arctic oscillation," *J. Clim.*, vol. 15, no. 18, pp. 2648–2663, Sep. 2002.

Aaron M. Swan was born in Corvallis, OR, in 1983. He received the B.Sc. and M.Sc. degrees in electrical engineering from Brigham Young University, Provo, UT, in 2009 and 2011, respectively.

From January 2008 to August 2008, he completed an internship as a Manageability Firmware Test Engineer with Hewlett Packard, Richardson, TX. After the completion of his B.Sc. degree, from August 2009 to August 2011, he was with the Microwave Earth Remote Sensing Laboratory, Brigham Young University, where he worked as a Research Assistant under Dr. D. G. Long. Since January 2011, he has been an Algorithms Engineer with ImSAR, Springville, UT.

David G. Long (S'80–SM'98–F'08) received the Ph.D. degree in electrical engineering from the University of Southern California, Los Angeles, in 1989.

From 1983 to 1990, he was with the Jet Propulsion Laboratory (JPL), National Aeronautics and Space Administration (NASA), Pasadena, CA, where he developed advanced radar remote sensing systems. While at JPL, NASA, he was the Project Engineer of the NASA Scatterometer project which flew from 1996 to 1997. He also managed the SCANSCAT project, the precursor to SeaWinds which was launched in 1999 on QuikSCAT and in 2002 on Advanced Earth Observing Satellite II. He is currently a Professor with the Department of Electrical and Computer Engineering, Brigham Young University (BYU), Provo, UT, where he teaches upper division and graduate courses in communications, microwave remote sensing, radar, and signal processing and is the Director of the BYU Center for Remote Sensing. He is the Principle Investigator of several NASA-sponsored research projects in remote sensing. He has over 400 publications in various areas, including signal processing, radar scatterometry, and synthetic aperture radar. His research interests include microwave remote sensing, radar theory, space-based sensing, estimation theory, signal processing, and mesoscale atmospheric dynamics.

Dr. Long has received the NASA Certificate of Recognition several times. He is an Associate Editor for IEEE GEOSCIENCE AND REMOTE SENSING LETTERS.